

ARTICLE OPEN



Effect of hydrogen on the passivation for ultra-thin 316 L SS foil

Xiaoqi Yue^{1,2}✉, Zhile Yang¹, Alfred Larsson³, Huajie Tang^{1,2}, Stephan Appelfeller⁴, Birhan Sefer⁵, Alexei Preobrajenski⁴, Jun Li⁶, Lei Zhang¹ and Jinshan Pan^{1,2}

The reformation and characterisation of the passive film formed on ultra-thin 316 L after hydrogen charging is investigated by combining EBSD, TMDs, XRD, Synchrotron-based XPS, and electrochemical experiments. The results show that ultra-thin foil reforms a passive film after 12 h of hydrogen release in NaCl solution. The reformed passive film is half the thickness of the as-received passive film and is dominated by Cr oxides/hydroxides. The lattice extension caused by residual hydrogen accelerates Cr migration to form Cr₂O₃; while the diffusible hydrogen occupies the cation vacancies and results in high defect density for the reformed passive film within 12 h.

npj Materials Degradation (2023)7:79; <https://doi.org/10.1038/s41529-023-00398-7>

INTRODUCTION

Nowadays, reducing the thickness of stainless steel (SS) foil appears as an effective solution to achieve the lightweight of precision component structures served in aggressive environments where Al foil is no longer suitable¹. TISCO Steel first manufactured the SS foil as thin as 0.02 mm, which showed bright application prospects². Strong and ductile features for ultra-thin 316 L SS foil that show potential with high resistance to corrosion and hydrogen embrittlement are essential for realising safety-critical energy components, hydrogen production industries, and flexible display solutions. For example, in the process of clean energy generation, the ultra-thin 316 L SS foil can be used as the flexible substrate and functional wrapping layers.

316 L SS with a face-centre-cubic (FCC) austenite structure has been reported to have a high solubility for hydrogen³, thus shows relatively low hydrogen embrittlement susceptibility, compared with materials with body-centre cubic (BCC) structure, such as martensitic⁴ and ferrite⁵ SSs. However, it has been noticed that hydrogen can adversely affect the passive film formation and pitting susceptibility of SS. Many studies have observed an increase in passive current density after the introduction of hydrogen^{4,6–9}. As an amorphous nanoscale surface film, the passive film of 316 L SS consists of inner oxides and outer hydroxides^{10,11}. Notably, the oxide layer acts as an effective barrier against corrosive ions^{12,13}. The reduction of oxide caused by cathodic polarisation during hydrogen charging has been widely known⁶, which corresponded to the passive film with a high density of defects in that period. The point defect model (PDM) suggests that the generation of defects enhances ionic transport across the oxide film, explaining why under some corrosive conditions, 316 L SS may lose passivity^{14,15}. Furthermore, it has been suggested that the diffusion of hydrogen away from the substrate to the film can accelerate the anodic dissolution after hydrogen charging⁸. Hydrogen was proposed to deteriorate the stability of the passive film by enhancing the deprotonation (removal of a proton)⁹, thus rendering the passive film less protective. The resistance to pitting affected by hydrogen was suggested to be more related to chromium, the reformed passive film^{16,17}.

Recently, the prominent passivation behaviour of ultra-thin 316 L foil has been reported, showing a clean material (no obvious inclusions) with significantly lower passive current density and higher breakdown potential in NaCl solution than wrought 316 L¹⁸. The reduction of thickness involved multiple cold rolling and bright annealing procedures that induced fine grains, preferential {110} plane, high-angle boundaries, and the absence of harmful MnS in the microstructure¹⁸. All these features facilitate the formation of a continuous compact passive film on the surface and thus reduce susceptibility to pitting corrosion of the ultra-thin 316 L foil. The formation and nature of passive film on the surface are essential to its safety application considering the unique dimensions. However, no work has been done with ultra-thin 316 L foil with as-received passive film to focus on the influence of hydrogen charging on the corrosion resistance and passive film nature. This work investigates the knowledge gap for ultra-thin 316 L foil affected by hydrogen charging in NaCl solution. The microstructure and passive film reformation mechanism of ultra-thin 316 L foil after hydrogen charging are analysed by a combination of EBSD, TMDs, XRD, synchrotron-based XPS, and electrochemical experiments.

RESULTS

Microstructure and deformation for H charging sample

The microstructures of the ultra-thin 316 L SS foil before and after hydrogen charging at 5 mA cm⁻² are displayed in Fig. 1a–c. Several cold rolling processes reduce the thickness of the foil down to approximately 20 μm¹⁸ and produce an average grain size of 4 μm in microstructure, accompanied by many twin boundaries remarked as green lines (Supplementary Fig. 1a). Figure 1d–f shows the Kernel average misorientation (KAM) or local misorientation histogram for ultra-thin 316 L austenite SS foil before and after hydrogen charging. KAM is associated with a misorientation (less than 5°) between neighbours which belongs to the same grain¹⁹. The high KAM values belong to the hydrogen-charged 316 L foils and are seen in irregular grains. The localised

¹Institute of Advanced Materials and Technology, University of Science and Technology Beijing, Beijing 100083, China. ²Division of Surface and Corrosion Science, KTH Royal Institute of Technology, Stockholm 11428, Sweden. ³Division of Synchrotron Radiation Research, Lund University, Lund, Sweden. ⁴MAX IV Laboratory, Lund, Sweden. ⁵Swerim AB, Luleå, Sweden. ⁶Shanxi Taigang Stainless Steel Co., Ltd., Taiyuan, China. ✉email: xiaoqi@kth.se

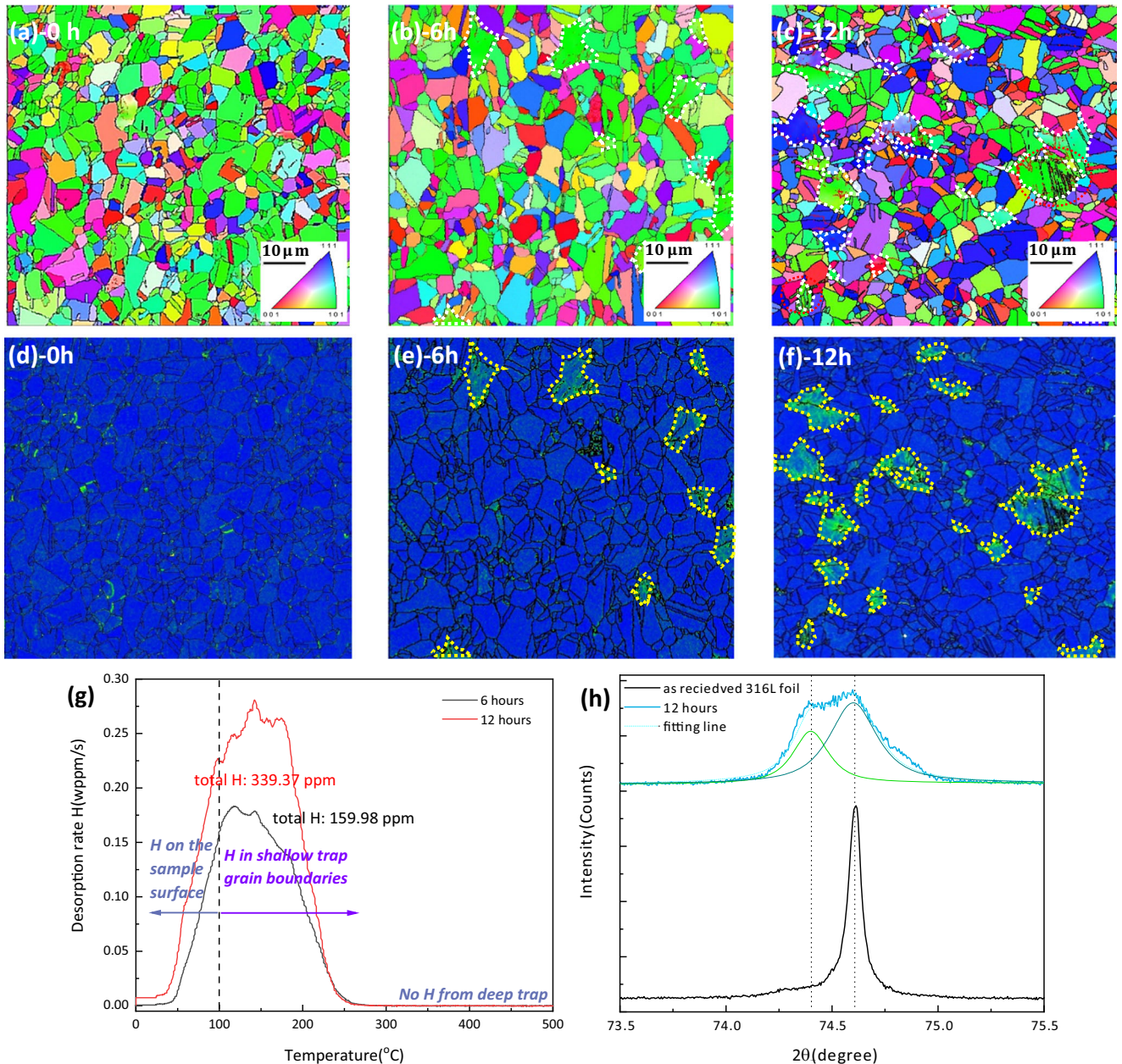


Fig. 1 Microstructure and deformation caused by hydrogen charging. **a–c** IPF Z map, **d–f** KAM maps, **g** TDMS patterns, and **h** XRD patterns for ultra-thin 316 L austenite SS foil before and after electrochemical hydrogen charge at -5 mA cm^{-2} in 3.5 wt% NaCl at pH 7.

distribution of high KAM value in Fig. 1e, f indicates the local plastic strain in ultra-thin 316 L austenite SS foil, especially near the grain boundaries of the orientation of (110). Besides, hydrogen was proposed to reduce the stacking fault energy²⁰, thus enhancing the dissociation of dislocations and the formation of stacking faults. Many parallel stacking faults arise in (110) grains with the infusion of H into ultra-thin 316 L SS foil, marked as red dash circles in Fig. 1c and Supplementary Fig. 1c, g shows the hydrogen desorption rate curves for ultra-thin 316 L austenite SS foil in 3.5 wt% NaCl solution for subsequent hydrogen charging times. With the increase of the hydrogen charging time from 6 to 12 h, the diffusible hydrogen content increased from 159.98 ppm to 339.27 ppm. Large and broad diffusible hydrogen peaks with many peak maxima indicate different trapping sites with varying binding energies. The distribution of diffusible hydrogen peaks (all

below 250 °C) indicates that the hydrogen is mainly located in shallow traps^{21,22}. However, the desorption of hydrogen tends to be at higher temperatures as hydrogen charging time progresses, indicating the potential for residual hydrogen after long-term hydrogen charging.

The residual hydrogen after hydrogen release can result in the subsequent lattice deformation that was detected via XRD patterns after 12 h of hydrogen release in 3.5 wt% NaCl solution. Fig. 1h illustrates the peak shift for the (110) phase, which shows a higher tendency of misorientation (Fig. 1f). 316 L foil shows a broadened peak with a larger full width at half maximum (FWHM) after 12 h of H charging at the position for (110), in comparison with a sharp and narrow peak before H charging. Near the original (110) peak, a broad peak arises, which represents the lattice expansion of the (110)-austenite. The average lattice deformation

induced by H at (110) was evaluated by Bragg's law as shown in Eq. (1):

$$2d \sin \theta = n\lambda \quad (1)$$

Where n is a positive integer, and λ is the wavelength of the incident X-ray wave. The lattice deformation of the (110) phase for 316 L SS foil was 0.24% according to the relationship between d -spacing and strain as follows:

$$\epsilon_{\text{lattice}} = \frac{d_{\text{H-charging}} - d_0}{d_0} = \frac{\sin \theta_0 - \sin \theta_{\text{H-charging}}}{\sin \theta_{\text{H-charging}}} \quad (2)$$

It has been proposed that the total dislocation density is dominated by geometrically necessary dislocation (GND) density as the true strain is below 6%²³, suggesting that the strain originates from the effective accumulation region shown in KAM maps in Fig. 1e, f. The inhomogeneous dislocations are considered reversible hydrogen traps where the hydrogen atoms can accumulate at their interfaces with the matrix and provide a pathway for atoms to move along these traps²⁴.

Passive film reformation after hydrogen charging

Figure 2a shows the potentiodynamic polarisation curves for the ultra-thin 316 L SS foil in 3.5 wt% NaCl solution after proceeding

with various hydrogen charging times. The passive current density increased from approximately 10^{-5} mA cm⁻² for the uncharged sample to a value of approximately 10^{-1} mA cm⁻² for the 12-h-charged sample. The increase in the passive current density is proposed to be attributed to the fact that the hydrogen charging procedure modified the passive film composition¹³. As shown in Fig. 2b, the pitting potentials decreased from 735 mV to 587 mV vs. Ag/AgCl with the increase of charging time from 0 to 12 h, combined with the dramatic decrease of corrosion potential from 51 mV to -614 mV vs. Ag/AgCl. It should be noted that the deterioration of passive current density and pitting corrosion potential has already significantly occurred after 4 h of charging. Many studies have proposed that the passive film can dissolve by reduction reactions during the hydrogen charging at cathodic polarisation^{25,26}. After stopping hydrogen charging, the reformation of the passive film can occur on the matrix with residual hydrogen, accompanied by the diffusible hydrogen away from the matrix, which may impact the reformation of the passive film.

Figure 2c shows the electrochemical impedance evolution of the ultra-thin 316 L SS foil after 12 h of H charging and subsequent hydrogen release periods in 3.5 wt% NaCl at pH 7 over 24 h of immersion. After 200 s of hydrogen release, the impedance exhibits a relatively small semi-arc and a diffusion tail at low frequencies. This indicates hydrogen desorption at the metal and

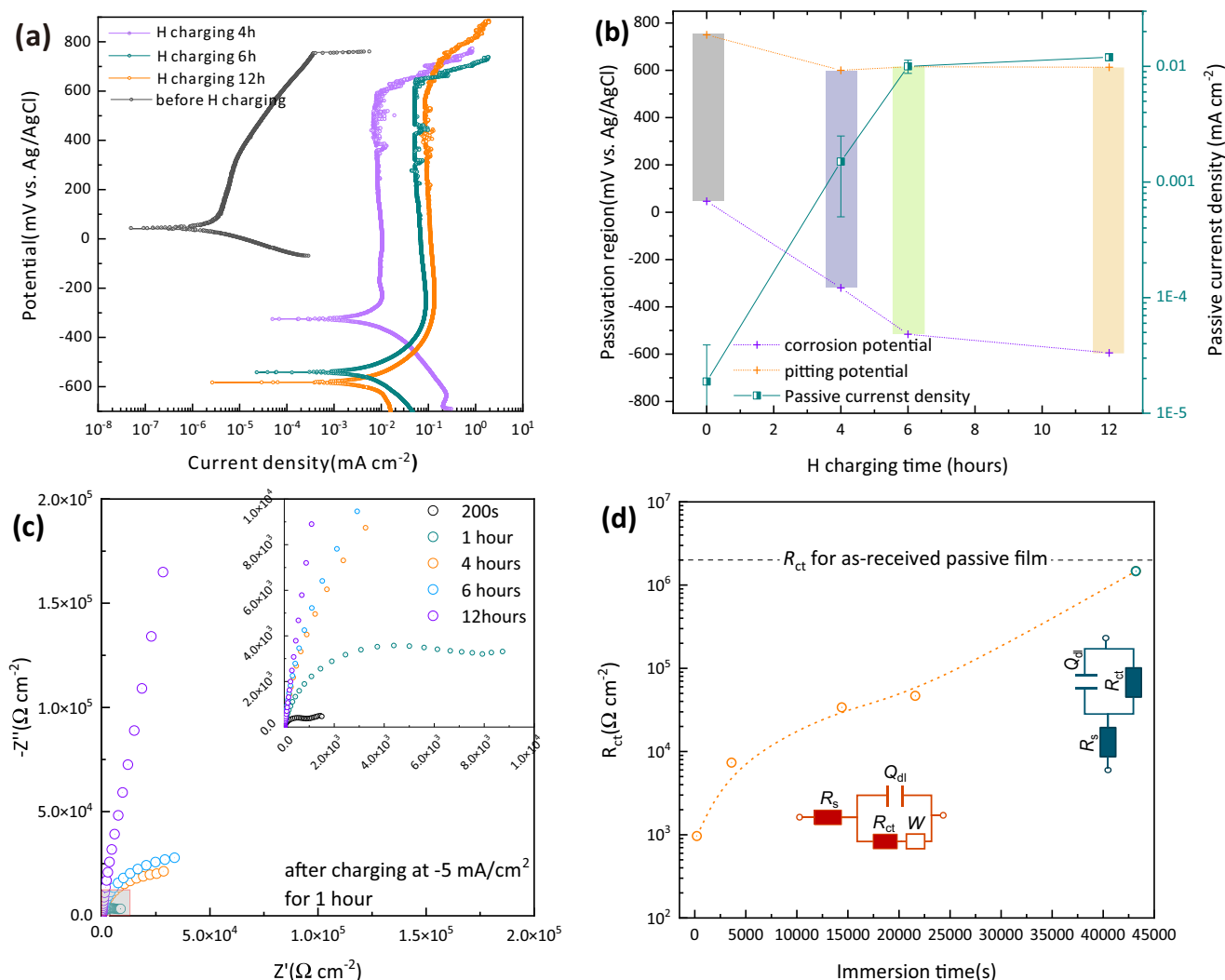


Fig. 2 Electrochemical characteristics after hydrogen charging. **a** Plots of potential dynamic curves, **b** the corrosion potential, corrosion current density, and pitting potentials for ultra-thin 316 L austenite SS foil after different H charging periods; **c** Nyquist and **d** charge transfer resistance for ultra-thin 316 L austenite SS foil after 12 h of H charging and subsequent hydrogen release periods in 3.5 wt% NaCl at pH 7.

solution interface. The semi-arc gradually increased as the immersion time prolonged, which indicates the reformation of the passive film against corrosion. As shown in Fig. 2d and Supplementary Table 1, upon 12 h of immersion, the impedance value reached the magnitude of the as-received passive film, with the diffusion tail disappearing, indicating that there is no diffusible hydrogen remaining in the matrix and only residual hydrogen that causes lattice expansion is left.

As stated above, the impedance of passive film on ultra-thin 316L SS foil in the experimental solution was restored after H release in an immersion period of 12 h. A comparison was made between the reformed passive film in the aqueous phase with the as-received passive film in its as-received state using flexible photoelectron spectroscopy (FlexPES), where detection was done with varying surface sensitivity by different photon energy (soft X-rays with a photon energy of 300–1450 eV, Supplementary Table 2). All spectra were calculated using the fermi level for specific levels at different photon energies.

Figure 3 shows the XPS spectra of the as-received sample and sample covering reformed passive film, respectively. For the chosen photon energy range, the detection depth is increased for higher photon energy. As shown in Fig. 3a, b, the intensity of the oxide peak increases at higher photon energy; whereas the hydroxide peaks are more surface sensitive, showing high intensity at low photon energy. This indicates the outer layer of the passive film is rich in hydroxides, while the inner layer is dominated by oxides. Hydroxides are present in high proportions in the outer layer of the reformed film in all detection depths when compared with the as-received passive film, indicating the composition and structure of passive film change on the matrix with lattice extension by residual hydrogen.

As shown in Fig. 3c, d, the high-resolution spectra of Fe 2p^{3/2} ionisation reveal Fe in the metallic state (707.1 eV), Fe^{II} (709.8 eV) and Fe^{III} (710.8 eV) in oxide form, and Fe^{III} in the form of hydroxides (711.8 eV)^{27,28}. As a Fe-based SS, the detection of the Fe⁰ peak indicates the detection depth has penetrated the entire passive film and reached the matrix. The Fe⁰ peaks can be detected at 807 eV photon energy for the reformed passive film in Fig. 3d, which suggests that the reformed passive film is thinner than the as-received passive film. Fig. 3e, f illustrate the spectra of Cr 2p^{3/2}, which can be split into Cr⁰ (574.1 eV), Cr₂O₃ (576.4 eV), and Cr(OH)₃ (577.2 eV)^{29,30}. However, it is noted that three compounds are not enough to fit the curve, therefore the CrN (575.7 eV) was introduced to fill the valley between metallic and oxidation states, which is consistent with the chemical composition showing the addition of N in the matrix. In addition, the signals obtained from Mo and Ni depress after the charging procedure, as shown in Supplementary Fig. 3a–d, respectively. In the reformed passive film, Ni and Mo compounds appear in relatively lower valence states than as-received passive film.

By quantitatively analysing, the composition of the outer hydroxide layer, inner oxide layer, and it is beneath the metallic layer of as-received and reformed passive film was calculated, as shown in Fig. 4.

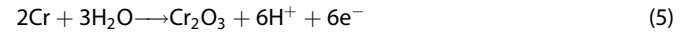
As seen in Fig. 4a, b, the Cr(OH)₃ content decreases and the Fe(OH)₃ content increases for both passive film as approaches the interface with aqueous. The Fe(OH)₃ dominates the outer layer of the as-received passive film, whereas the reformed passive film shows a high composition of Cr(OH)₃, which implies that the formation of Cr(OH)₃ by the following reactions was enhanced:



Furthermore, the outer layer of the reformed passive film also shows significant changes in Ni compounds, despite their scarcity. The distribution of Ni hydroxide in the as-received passive film

was near the interface with the oxide layer. However, it was detected near the interface with aqueous in the reformed passive film.

As for the oxide layer shown in Fig. 4c, d, the reformed passive film contains a higher composition of Cr oxides than the as-received passive film, indicating the acceleration of the following reaction:



Besides, the composition of molybdenum oxides was relatively higher for the reformed passive film, which was also observed for the reformation after passive film breakdown^{29,30}.

As seen in Fig. 4e, f, Ni is enriched in the metallic layer beneath both the as-received and the reformed passive film, however, it is more abundant within the metallic layer beneath the reformed passive film, which can be related to the consumption of Cr and Fe during the reforming process. The depletion of Cr is particularly evident at the interface with the oxide layer of the reformed passive film, indicating that the promotion of forming Cr compounds can be attributed to the accelerated Cr migration in the matrix with lattice extension.

Moreover, the migration of Cr is also related to the minor amount of N in the matrix. As referred to in the works of literature^{31–34}, N has a high affinity for Cr, thus restricting the migration of Cr. Fig. 5a compares the N 1s spectra for a-received passive film and reformed passive film at 1000 eV photon energy, where the peaks represent the formation of Cr–N and N–H bonds at 396.6 eV and 398.7 eV, respectively^{32,35–37}. It is noted that the proportion of Cr–N bond is reduced for the reformed passive film, whereas the Cr–H bond increases after hydrogen charging. The disruption of the Cr–N bond by hydrogen relieves the binding of N on Cr, thereby facilitating the migration of Cr.

Figure 5b shows the Mott–Schottky plots for the as-received passive film of ultra-thin 316L SS foil and the reformed passive film in the various hydrogen release periods, and the space-charge capacitance (*C*) of the defective semiconductor can be expressed as follows:

$$\frac{1}{C^2} = \frac{2}{\epsilon\epsilon_0 e N_D} \left(E - E_{fb} - \frac{kT}{e} \right) \text{ n-type} \quad (6)$$

$$\frac{1}{C^2} = \frac{2}{\epsilon\epsilon_0 e N_A} \left(E - E_{fb} - \frac{kT}{e} \right) \text{ p-type} \quad (7)$$

where ϵ is the dielectric constant of the passive film, usually taken as 15.6³⁸, ϵ_0 is the permittivity of vacuum ($8.854 \times 10^{-12} \text{ F m}^{-1}$), e is the electron charge ($1.60 \times 10^{-19} \text{ C}$), k is the Boltzmann constant and T is the absolute temperature; N_D and N_A represent the donor density for n-type semiconductor and acceptor density for p-type semiconductor, E_{fb} represents the flat band potential.

As for the as-received passive film, the positive slopes of the experimental C^{-2} vs. E plots indicated the n-type semiconductor properties, which are mainly dominated by oxygen vacancies or interstitial metals as defections in passive film. However, the N_D increases for the reformed passive film, especially in the early periods (200 s–1 h), which suggests the increase in defects for the reformed passive film after hydrogen charging. Yang et al.³⁹ reported that hydrogen atoms can increase the N_D by entering the passive film and increasing the degree of compositional disorder. This accounts for the hydrogen-induced increase of the passive current density, as shown in Fig. 2b.

It is noted that the negative slopes were obtained in the relatively negative potential region, which indicated the p-type semiconductor properties and therefore developed for a single p–n junction, which is consistent with the results from Örnek et al.⁴⁰. The p-type semiconductors correspond to the layer dominated by chromium oxide with cation vacancies, while n-type semiconductors correspond to the layer dominated by iron oxide

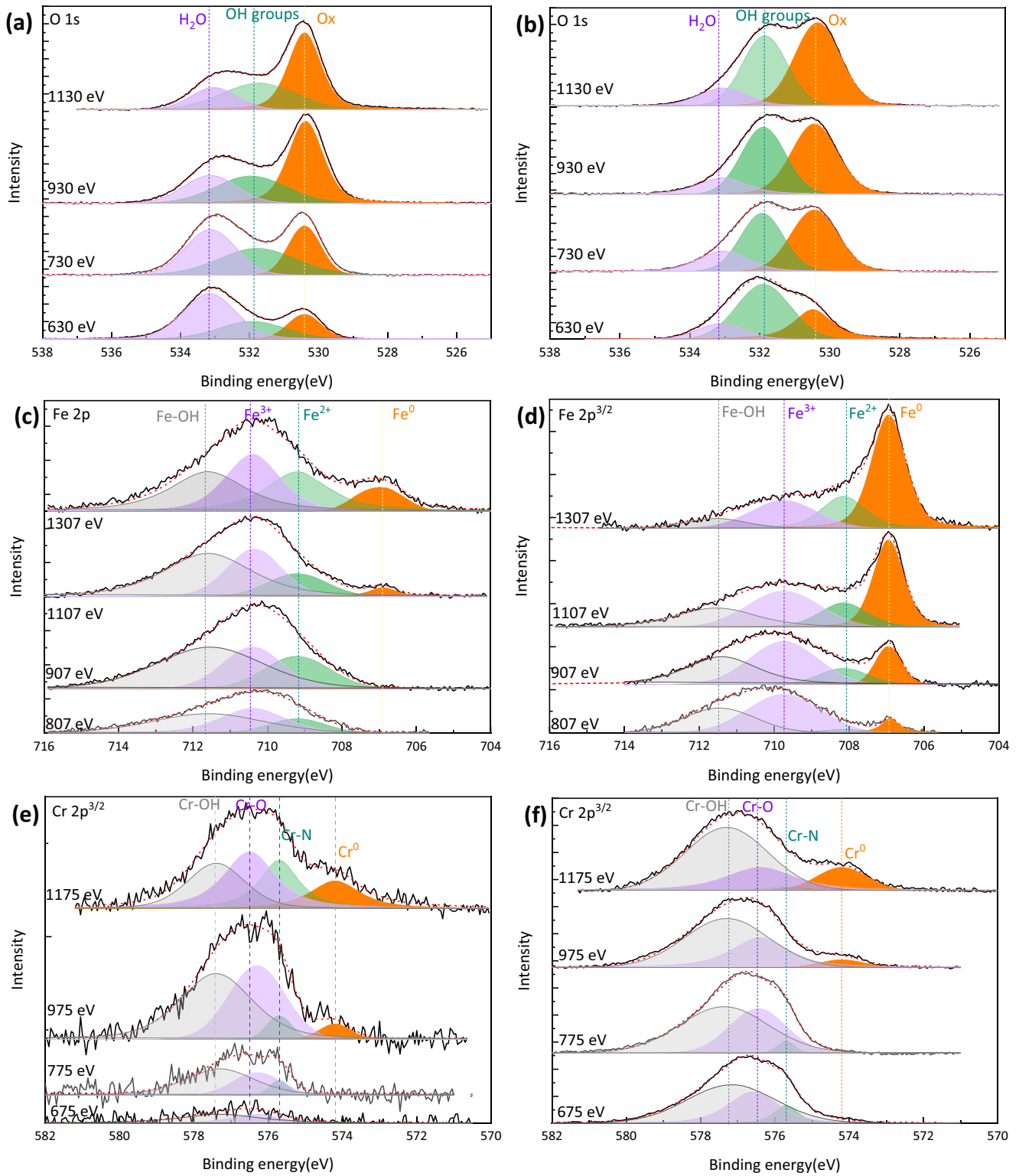


Fig. 3 Surface chemistry of the primary elements under kinetic energy for 100- 600 eV. a, b O 1 s, c, d Fe 2p^{3/2}, and e, f Cr 2p^{3/2} XPS spectra of the as-received passive film (left) and reformed passive film after hydrogen charging (right) on ultra-thin 316 L austenite SS foil.

with oxygen vacancies^{36,41–43}. The results in Fig. 5b indicate that the as-received passive film is dominated by Fe oxides, which matches the results detected by XPS. The apparent donor density of the as-received passive film is $4.23 \times 10^{21} \text{ cm}^{-3}$, which matches the published results for 316 L SS^{18,44–46}.

After stopping hydrogen charging, hydrogen escapes from the material and affects the reforming of the passive film. As shown in Supplementary Table 3, the high acceptor density dominated the defects in re-formed passive film, especially in the early period. The hydrogen atoms were proposed to enter

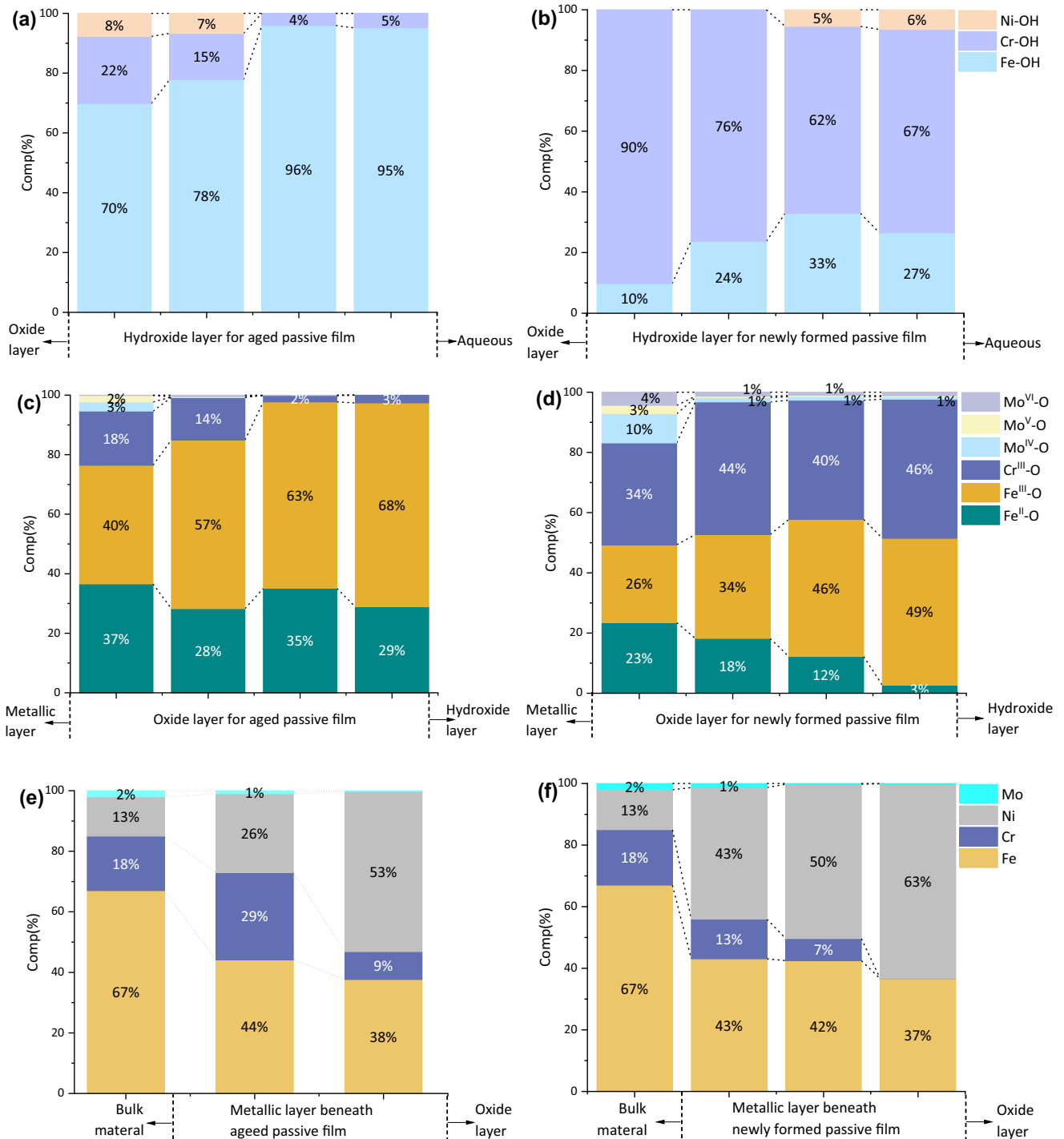


Fig. 4 Surface chemistry changes after hydrogen charging. Composition of the outer hydroxide layer (a, b) and the inner oxide layer (c, d) of the as-received passive film (left column) and reformed passive film (right column) after hydrogen charging on ultra-thin 316 L austenite SS foil; and beneath metallic layer (e, f).

into the Cr vacancy of Cr_2O_3 and bond with the surrounding O^{16} . However, the formation of vacancies by the interaction of O–H is difficult to detect since it shows the indistinguishable binding energy (BE) as hydroxides. It is worth noting that the ultra-thin 316 L foil sample was doped with a trace amount of N, which can bond with hydrogen. The high intensity of the N–H bond explained the appearance of acceptors for the reformed passive film.

DISCUSSION

Based on the above analyses, the iron oxides, combined with inner Mo oxides and chromium oxide doping with nitrogen, play a decisive role in the corrosion resistance of the as-received passive film. During the hydrogen changing procedure, the as-received passive film was removed by cathodic polarisation (around -1.6 V vs. Ag/AgCl). The reformation of the passive film occurred and was combined with the release of diffusible hydrogen after stopping

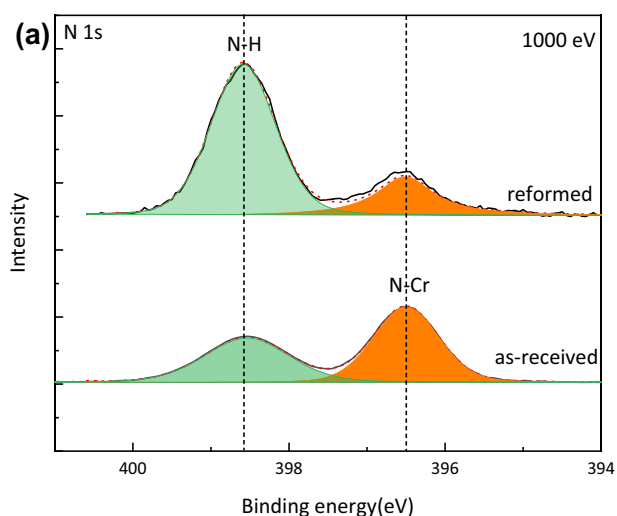


Fig. 5 Defective structure after hydrogen charging. **a** N 1s XPS spectra, and **b** Mott–Schottky plots of the as-received passive film and reformed passive film after hydrogen charging on ultra-thin 316 L austenite SS foil.

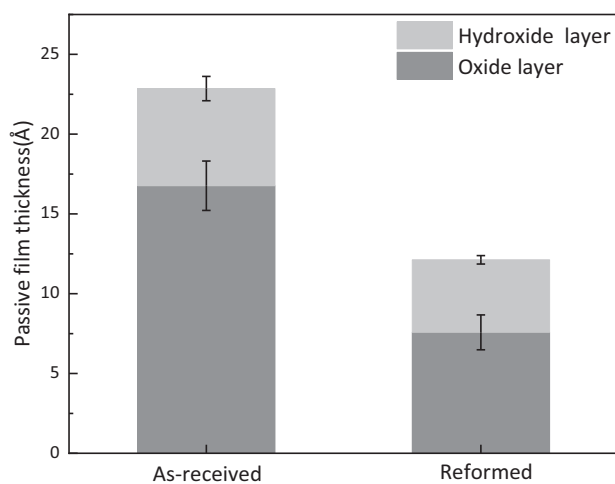
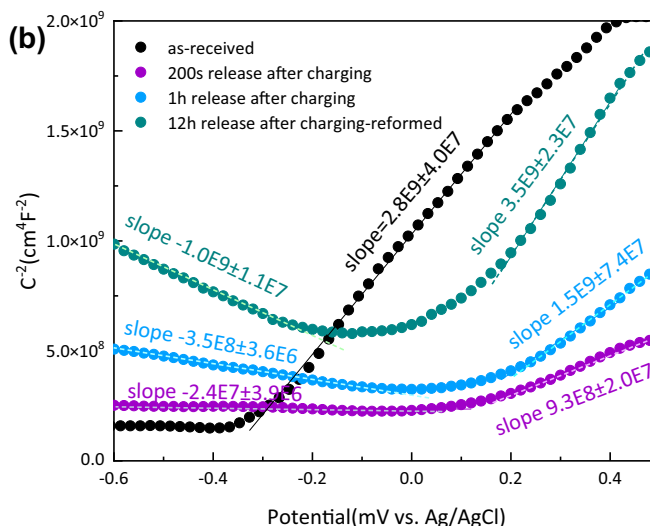


Fig. 6 Film thickness changes after hydrogen charging. The thickness of the as-received and reformed passive film by normalisation of PES results. For both oxide and hydroxide layers, error bars indicate the mean standard deviation of the thickness calculated from varying oxides and hydroxides.

hydrogen charging. The diffusible hydrogen occupied cation vacancies and resulted in high acceptor density for reformed passive film in the early period; while the residual hydrogen caused the lattice extension of the matrix and accelerated the migration of cations. The activation energy for migration of Cr was reported to be the lowest, followed by Fe, Ni and then Mo^{47,48}, so Cr migration was more promoted, forming Cr₂O₃. Furthermore, compared with bulk 316 L SS, the microstructure of the ultra-thin 316 L foil was characterised by fine grain size with more high-angle grain boundaries, more favourable {110} grain orientation, generation of stacked dislocations, fine oxide inclusions, and absence of harmful MnS inclusions¹⁸. As a result of hydrogen charging, stacking faults are formed in (110) grains (Fig. 1e, f) in which Cr diffuses more quickly than Fe or Ni⁴⁷ and forms Cr₂O₃ with a higher BE than other orientations⁴⁹. Figure 6 presents the thickness of the as-received and reformed passive film (calculated by normalisation of PES results). The thickness of the reformed passive film is much thinner than the as-received passive film, especially for the oxide layer. One one hand, the lattice extension



accelerates the migration of cations to form oxides, especially for Cr. On the other hand, the high density of defects caused by diffusible hydrogen renders the reformed passive film more permeable to ion transport (higher dissolution rate), which would allow the film to reach an equilibrium composition faster (at the thinner condition).

Figure 7 illustrates the schematically of hydrogen effects on the reformation of the passive film of ultra-thin 316 L SS foil. Most hydrogen was found to be diffusible and affected the early period of passive film reformation. A minor amount of residual hydrogen was found to induce lattice extension in a small range, which accelerates the migration of cations to reform a passive film, especially for Cr. The thermodynamic calculation shown in Supplementary Fig. 4 indicates that the metallic phases are thermodynamically stable in the hydrogen charging region, corresponding to the removal of the oxide layer. Based on the results of R_{ct} in Fig. 2c, the surface oxide film reforms when electrochemical hydrogen charging is stopped. As the passive film reforms, the potential rises from the cathode region to the corrosion potential. For the samples after 12 h of hydrogen charging, the corrosion potential is -597 mV vs. Ag/AgCl (-400 mV vs. SHE), as shown in Fig. 2a. From the hydrogen charging region to the corrosion potential marked in Supplementary Fig. 4, the migration of Cr to form Cr oxides first becomes thermodynamically favourable (at relatively low potential), followed by Fe and then Mo, consistent with the Cr₂O₃-dominated film shown in XPS results (Fig. 4d). The diffusible hydrogen can be caught by the subsequently formed Cr₂O₃ by entering Cr vacancies, showing a high defect density. However, defect density was decreased as the hydrogen release time was prolonged, which can be attributed to the enhancement of Cr₂O₃ formation by lattice extension from residual hydrogen. In this paper, we recorded the thickness of the reformed passive film after 12 h of hydrogen release and found it was half thinner than the received passive film. However, we can assume that as the immersion time prolong, all the hydrogen-occupied parts of the re-formed passive film would dissolve. And the Cr₂O₃ formation rate remains high, which would allow the film to reach an equilibrium composition with the thicker condition.

In summary, the characteristics of passive film and microstructure of ultra-thin 316 L foil after hydrogen charging in 3.5 wt% NaCl solution has been compared with the as-received foil sample. The study focused on the reformation of passive films on the matrix affected by hydrogen charging, and the following main conclusions can be made:

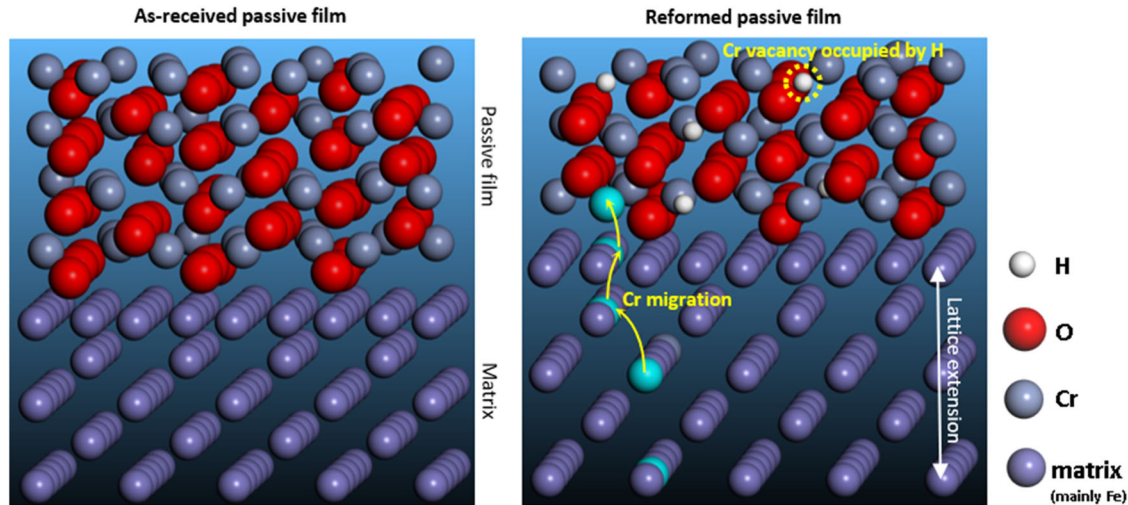


Fig. 7 Schematically of hydrogen effects on the reformation of passive film of ultra-thin 316 L SS foil. Residual hydrogen induces lattice extension and accelerates the Cr migration, while the diffusible hydrogen results in Cr vacancies in the reformed passive film.

- The reformation of passive film on ultra-thin foil in NaCl solution was affected by two kinds of hydrogen: I, the diffusible hydrogen released away from the matrix; II, the residual hydrogen caused lattice extension, especially in the orientation of (110). The diffusion of hydrogen can enter Cr vacancies and result in high defect density of reformed passive film; whereas the lattice extension accelerates the diffusion of Cr in the metallic layer to form Cr_2O_3 .
- The as-received passive film for ultra-thin foil mainly contains Fe oxides and hydroxides. However, after hydrogen charging, the reformed passive film is mainly comprised of Cr_2O_3 in the oxide layer and $\text{Cr}(\text{OH})_3$ in the hydroxide layer.
- The thickness of the reformed passive film after hydrogen charging is 12.5 Å and is only half the thickness of the as-received passive film. A thin oxide layer with high cation defects was the main reason for reaching an equilibrium composition with the thinner condition.

METHODS

Material and methods

The test material used was an ultra-thin 316 L SS foil supplied by TISCO Steel from China with I chemical composition (wt%): C 0.016%, Si 0.45%, Mn 1.18%, Cr 17.17%, Ni 12.14%, Mo 2.10%, N 0.10%, S \leq 0.001%, P \leq 0.001%, and Fe balance. The material was thinned from raw material (1 mm) to foil (20 μm) through five cold rolling passes, followed by bright annealing after each cold rolling. The surface roughness (R_a) of the as-received ultra-thin 316 L foil is approximately 0.2. The species with a dimension of 20 mm, 310 mm and 320 μm were used for electrochemical tests and subsequent synchrotron-based X-ray photoelectron spectroscopy study.

Thermal desorption spectroscopy with mass spectrometry (TDMS) was applied to perform the diffusible hydrogen analysis for samples after different hydrogen charging time foils by heating the foils from room temperature to 600 °C using a heating rate of 0.33 °C s⁻¹. The samples were stored in liquid nitrogen before TDMS tests.

After 12 h of hydrogen release, electron backscatter diffraction (EBSD) was carried out on foil specimens using a Nordlys MAX3 (OXFORD) instrument to assess the microstructure before and after hydrogen charging. The orientation of interest was selected based on the KAM, which measured the local grain misorientation. All the information was collected with a high-resolution CCD of

6403480 pixels. Further, the lattice extension caused by residual hydrogen for specific orientation was conducted via X-ray diffraction (XRD) spectrum after 12 h of hydrogen release using Cu K α radiation with an active area of 10 mm \times 10 mm, employing a step size of 0.0048°.

Electrochemical tests

The hydrogen charging experiments were carried out with a Pt counter electrode and Ag/AgCl reference electrode in 3.5 wt% NaCl solution at pH 7 and ambient temperature, using a Gamry reference 600+ workstation. For the austenite phase, the solubility of atomic hydrogen is high due to the abundant occupation sites (octahedral voids), which induce mutative microplastic deformation for austenite grains (20 μm depth) within 9.5 h⁶. A constant cathodic current density of 5 mA cm⁻² was applied for a period from 4 to 12 h. After the hydrogen charging procedure, the samples were stored in liquid nitrogen for subsequent analyses, followed by other electrochemical tests in 3.5 wt% NaCl solution, including potentiodynamic polarisation, electrochemical impedance spectroscopy (EIS), and Mott–Schottky plot. The potentiodynamic polarization measurements were conducted from 0.1 V vs. OCP with a sweep rate of 0.127 mV s⁻¹. The potentiodynamic polarisation needs to terminate in a short period after breakdown potential otherwise, it will be perforated. The EIS measurements were performed from 100 kHz to 10 mHz with 10 mV sinusoidal potential modulation in a potentiostatic condition. The Mott–Schottky plots were measured with 100 Hz and 10 mV sinusoidal potential from the passivation region to the cathodic region with a rate of 20 mV s⁻¹. The open circuit potential (OCP) was recorded before the tests in both potentiodynamic/potentiostatic conditions. The OCP values were measured for 200 s after hydrogen charging, followed by the measurement of 600 s.

Synchrotron-based X-ray photoelectron spectroscopy study

The XPS experiments were conducted at the FlexPES beamline at MAX IV Laboratory, Lund, Sweden⁵⁰. The tunable energy at modern synchrotron facilities allows the photon energy to be varied such that the kinetic energy of the photoelectrons is the same for each core level. Here the photon energy was chosen such that the kinetic energy was conducted at 100, 200, 400, and 600 eV for each core level separately. This results in a constant probing depth of the XPS signal from each alloying element. The probing depth can be calculated from the inelastic mean free path of the electrons⁵¹. A survey spectrum was measured at 1200 eV for

each sample, followed by high-resolution spectra collected at the following core levels: Ni 2p, Fe 2p, Cr 2p, O 1s, Mo 3d, and N 1s. A summary of the core levels and the respective photon energy used are listed in Supplementary Table 2. The BE for each spectrum was calibrated against the measured Fermi edge.

DATA AVAILABILITY

The datasets used and/or analysed during the current study are available from the corresponding author upon reasonable request.

Received: 4 May 2023; Accepted: 29 September 2023;

Published online: 10 October 2023

REFERENCES

- Xia, L. China's TISCO boasts research, development of high-tech stainless steel products. http://www.xinhuanet.com/english/2019-06/04/c_138116414_9.htm (2019).
- TISCO's wide ultra-thin precision stainless steel strip to be used in Chinese foldable screen mobile phone. <http://www.asianmetal.com/news/data/1512149/TISCO's%20wide%20ultra-thin%20precision%20stainless%20steel%20strip%20to%20be%20used%20in%20Chinese%20foldable%20screen%20mobile%20phone>.
- He, J. et al. A novel 13Cr austenitic stainless steel with excellent mechanical properties and high hydrogen embrittlement resistance via heterostructure and TRIP effects. *Mater. Sci. Eng. A* **793**, 139835 (2020).
- He, J. et al. Hydrogen embrittlement behavior of 13Cr-5Ni-2Mo supermartensitic stainless steel. *Corros. Sci.* **176**, 109046 (2020).
- Guo, L. Q. et al. Effect of hydrogen on pitting susceptibility of 2507 duplex stainless steel. *Corros. Sci.* **70**, 140–144 (2013).
- Örnek, C. et al. Operando time-and space-resolved high-energy X-ray diffraction measurement to understand hydrogen-microstructure interactions in duplex stainless steel. *Corros. Sci.* **175**, 108899 (2020).
- Yashiro, H., Pound, B., Kumagai, N. & Tanno, K. The effect of permeated hydrogen on the pitting of type 304 stainless steel. *Corros. Sci.* **40**, 781–791 (1998).
- Wallinder, D., Hultquist, G., Tveten, B. & Hörlund, E. Hydrogen in chromium: influence on corrosion potential and anodic dissolution in neutral NaCl solution. *Corros. Sci.* **43**, 1267–1281 (2001).
- Ningshen, S. et al. Hydrogen effects on the passive film formation and pitting susceptibility of nitrogen containing type 316L stainless steels. *Corros. Sci.* **48**, 1106–1121 (2006).
- Yue, X., Zhang, L., He, X., Kong, D. & Hua, Y. Hypo-toxicity and prominent passivation characteristics of 316 L stainless steel fabricated by direct metal laser sintering in a simulated inflammation environment. *J. Mater. Sci. Technol.* **93**, 205–220 (2021).
- Kong, D. et al. The passivity of selective laser melted 316L stainless steel. *Appl. Surf. Sci.* **504**, 144495 (2020).
- Luo, H., Dong, C., Xiao, K. & Li, X. The passive behaviour of ferritic stainless steel containing alloyed tin in acidic media. *RSC Adv.* **6**, 9940–9949 (2016).
- Luo, H. et al. Hydrogen effects on microstructural evolution and passive film characteristics of a duplex stainless steel. *Electrochim. Commun.* **79**, 28–32 (2017).
- Macdonald, D. D. The history of the point defect model for the passive state: a brief review of film growth aspects. *Electrochim. Acta* **56**, 1761–1772 (2011).
- Zhong, J., Mao, F., Ghanbari, E. & Macdonald, D. D. Passivity breakdown on 300 M and S280 ultra-high strength steels in borate buffer solutions containing chloride ion. *Electrochim. Acta* **251**, 324–335 (2017).
- Mi, Z. et al. Prevent hydrogen damage in α -Cr₂O₃/ α -Fe₂O₃ (0 0 0 1) interface. *Appl. Surf. Sci.* **475**, 294–301 (2019).
- Nigussa, K., Nielsen, K., Borck, Ø. & Støvneng, J. Adsorption of hydrogen, chlorine, and sulfur atoms on α -Cr₂O₃ (0 0 0 1) surfaces: A density functional theory investigation. *Corros. Sci.* **53**, 3612–3622 (2011).
- Yue, X. et al. Passivation characteristics of ultra-thin 316L foil in NaCl solutions. *J. Mater. Sci. Technol.* **127**, 192–205 (2022).
- Badji, R., Chauveau, T. & Bacroix, B. Texture, misorientation and mechanical anisotropy in a deformed dual phase stainless steel weld joint. *Mater. Sci. Eng. A* **575**, 94–103 (2013).
- Kong, D. et al. Superior resistance to hydrogen damage for selective laser melted 316L stainless steel in a proton exchange membrane fuel cell environment. *Corros. Sci.* **166**, 108425 (2020).
- Wei, F., Hara, T. & Tsuzuki, K. Precise determination of the activation energy for desorption of hydrogen in two Ti-added steels by a single thermal-desorption spectrum. *Metall. Mater. Trans. B* **35**, 587–597 (2004).
- Wei, F. G. & Tsuzuki, K. Quantitative analysis on hydrogen trapping of TiC particles in steel. *Metall. Mater. Trans.* **37**, 331–353 (2006).
- Zhi, H. et al. Investigations of dislocation-type evolution and strain hardening during mechanical twinning in Fe-22Mn-0.6 C twinning-induced plasticity steel. *Acta Mater.* **195**, 371–382 (2020).
- Mohtadi-Bonab, M., Eskandari, M. & Szpunar, J. Texture, local misorientation, grain boundary and recrystallization fraction in pipeline steels related to hydrogen induced cracking. *Mater. Sci. Eng. A* **620**, 97–106 (2015).
- Långberg, M. et al. Redefining passivity breakdown of super duplex stainless steel by electrochemical operando synchrotron near surface X-ray analyses. *npj Mater. Degrad.* **3**, 1–11 (2019).
- Örnek, C. et al. Metastable precursor structures in hydrogen-infused super duplex stainless steel microstructure—An operando diffraction experiment. *Corros. Sci.* **176**, 109021 (2020).
- Gardin, E., Zanna, S., Seyeux, A., Allion-Maurer, A. & Marcus, P. XPS and ToF-SIMS characterization of the surface oxides on lean duplex stainless steel—Global and local approaches. *Corros. Sci.* **155**, 121–133 (2019).
- Yamashita, T. & Hayes, P. Analysis of XPS spectra of Fe²⁺ and Fe³⁺ ions in oxide materials. *Appl. Surf. Sci.* **254**, 2441–2449 (2008).
- De Vito, E. & Marcus, P. XPS study of passive films formed on molybdenum-implanted austenitic stainless steels. *Surf. Interface Anal.* **19**, 403–408 (1992).
- Wang, Z. et al. XPS and ToF-SIMS investigation of native oxides and passive films formed on nickel alloys containing chromium and molybdenum. *J. Electrochem. Soc.* **168**, 041503 (2021).
- Park, J. W., Rao, V. S. & Kwon, H. S. Effects of nitrogen on the repassivation behavior of type 304L stainless steel in chloride solution. *Corrosion* **60**, 1099–1103 (2004).
- Marcus, P. & Bussell, M. E. XPS study of the passive films formed on nitrogen-implanted austenitic stainless steels. *Appl. Surf. Sci.* **59**, 7–21 (1992).
- Feng, H. et al. Influence of nitrogen on corrosion behaviour of high nitrogen martensitic stainless steels manufactured by pressurized metallurgy. *Corros. Sci.* **144**, 288–300 (2018).
- Dai, J. et al. Nitrogen significantly enhances corrosion resistance of 316L stainless steel in thiosulfate-chloride solution. *Corros. Sci.* **174**, 108792 (2020).
- Willenbruch, R., Clayton, C., Oversluizen, M., Kim, D. & Lu, Y. An XPS and electrochemical study of the influence of molybdenum and nitrogen on the passivity of austenitic stainless steel. *Corros. Sci.* **31**, 179–190 (1990).
- Ningshen, S., Kamachi Mudali, U., Mittal, V. K. & Khatak, H. S. Semiconducting and passive film properties of nitrogen-containing type 316LN stainless steels. *Corros. Sci.* **49**, 481–496 (2007).
- Ha, H., Jang, H., Kwon, H. & Kim, S. Effects of nitrogen on the passivity of Fe–20Cr alloy. *Corros. Sci.* **51**, 48–53 (2009).
- Li, D., Wang, J., Chen, D. & Liang, P. Influences of pH value, temperature, chloride ions and sulfide ions on the corrosion behaviors of 316L stainless steel in the simulated cathodic environment of proton exchange membrane fuel cell. *J. Power Sources* **272**, 448–456 (2014).
- Yang, M. et al. Effects of hydrogen on semiconductivity of passive films and corrosion behavior of 310 stainless steel. *J. Electrochem. Soc.* **146**, 2107 (1999).
- Örnek, C. et al. Understanding passive film degradation and its effect on hydrogen embrittlement of super duplex stainless steel—synchrotron X-ray and electrochemical measurements combined with CalPhaD and ab-initio computational studies. *Appl. Surf. Sci.* **628**, 157364 (2023).
- de Oliveira, R. K., Correa, O. V., de Oliveira, M. C. L. & Antunes, R. A. Surface chemistry and semiconducting properties of passive film and corrosion resistance of annealed surgical stainless steel. *J. Mater. Eng. Perform.* **29**, 6085–6100 (2020).
- Azumi, K., Ohtsuka, T. & Sato, N. Mott-Schottky plot of the passive film formed on iron in neutral borate and phosphate solutions. *J. Electrochem. Soc.* **134**, 1352 (1987).
- Darowicki, K., Krakowiak, S., & Ślepski, P. Selection of measurement frequency in Mott-Schottky analysis of passive layer on nickel. *Electrochim. Acta* **51**, 2204–2208 (2006).
- Duan, Z. et al. Pitting behavior of SLM 316L stainless steel exposed to chloride environments with different aggressiveness: Pitting mechanism induced by gas pores. *Corros. Sci.* **167**, 108520 (2020).
- Ding, J. et al. The electrochemical behaviour of 316L austenitic stainless steel in Cl⁻ containing environment under different H₂S partial pressures. *Appl. Surf. Sci.* **289**, 33–41 (2014).
- Fattah-alhosseini, A., Soltani, F., Shirsalimi, F., Ezadi, B. & Attarzadeh, N. The semiconducting properties of passive films formed on AISI 316 L and AISI 321 stainless steels: a test of the point defect model (PDM). *Corros. Sci.* **53**, 3186–3192 (2011).
- Middleburgh, S., King, D., Lumpkin, G., Cortie, M. & Edwards, L. Segregation and migration of species in the CrCoFeNi high entropy alloy. *J. Alloy. Compd.* **599**, 179–182 (2014).

48. Verma, A., Singh, J., Kaushik, S. & Siruguri, V. Lattice parameter variation and its effect on precipitation behaviour of ordered Ni₂(Cr, Mo) phase in Ni-Cr-Mo alloys. *J. Alloy. Compd.* **813**, 152195 (2020).
49. Yue, X. et al. Revealing the superior corrosion protection of the passive film on selective laser melted 316L SS in a phosphate-buffered saline solution. *Appl. Surf. Sci.* **529**, 147170 (2020).
50. Preobrajenski, A. et al. FlexPES: a versatile soft X-ray beamline at MAX IV Laboratory. *J. Synchrotron Radiat.* **30**, 831–840 (2023).
51. Larsson, A. et al. Thickness and composition of native oxides and near-surface regions of Ni superalloys. *J. Alloy. Compd.* **895**, 162657 (2022).

ACKNOWLEDGEMENTS

This work was supported by the National Natural Science Foundation of China (Grant No. 52101069), China Postdoctoral Science Foundation (No. 2021M690345), and the Swedish Foundation for International Cooperation in Research and Higher Education (STINT project for Swedish-China collaboration, grant No. CH2017-7255). We acknowledge MAX IV Laboratory for time on Beamline FlexPES under Proposal 20210800. Research conducted at MAX IV, a Swedish national user facility, is supported by the Swedish Research Council under contract 2018-07152, the Swedish Governmental Agency for Innovation Systems under contract 2018-04969, and Formas under contract 2019-02496.”)

AUTHOR CONTRIBUTIONS

X.Y.: Data curation, formal analysis, investigation, methodology, writing—original draft. Z.Y., A.L., and H.T.: Data curation, formal analysis, methodology, writing—review & editing. J.L.: Sample preparation. S.A. and A.P.: Surface analyses. B.S.: TDS analyses. J.P. and L.Z.: Conceptualisation, data curation, investigation, methodology, writing—original draft, supervision.

FUNDING

Open access funding provided by Royal Institute of Technology.

COMPETING INTERESTS

The authors declare no competing interests.

ADDITIONAL INFORMATION

Supplementary information The online version contains supplementary material available at <https://doi.org/10.1038/s41529-023-00398-7>.

Correspondence and requests for materials should be addressed to Xiaoqi Yue.

Reprints and permission information is available at <http://www.nature.com/reprints>

Publisher's note Springer Nature remains neutral with regard to jurisdictional claims in published maps and institutional affiliations.



Open Access This article is licensed under a Creative Commons Attribution 4.0 International License, which permits use, sharing, adaptation, distribution and reproduction in any medium or format, as long as you give appropriate credit to the original author(s) and the source, provide a link to the Creative Commons licence, and indicate if changes were made. The images or other third party material in this article are included in the article's Creative Commons licence, unless indicated otherwise in a credit line to the material. If material is not included in the article's Creative Commons licence and your intended use is not permitted by statutory regulation or exceeds the permitted use, you will need to obtain permission directly from the copyright holder. To view a copy of this licence, visit <http://creativecommons.org/licenses/by/4.0/>.

© The Author(s) 2023